AUTONOMOUS PRECISION TAKEOFF AND LANDING SYSTEM FOR VTOLS IN DEGRADED VISUAL AND GNSS DENIED ENVIRONMENTS

Christopher Doer[1], Ronja Koenig[2], Gert F. Trommer [1,3], Eike Stumpf[2]

[1] Institute of Control Systems (IRS), Karlsruhe Institute of Technology (KIT), Karlsruhe, 76131, Germany
[2] Institute of Aerospace Systems (ILR), RWTH Aachen University, Aachen, 52062, Germany
[3] Department of Information and Navigation Systems, ITMO University, Saint Petersburg, Russia

Abstract

Vertical Takeoff and Landing Systems (VTOLs) offer huge potential for various use cases. During the critical flight phases of takeoff and landing, a safe and reliable flight operation is crucial. This paper presents an autonomous precision takeoff and landing system based on thermal imaging. As thermal imaging is not affected by poor visibility, safe and reliable navigation is enabled. Inspired by visual approaches, a landing platform with thermal makers is developed. A downfacing thermal camera detects the landing platform and enables precision takeoff and landing. The proposed system is evaluated in simulation and in testflights with a motion capture system. Demonstrations in bad visual conditions prove the approach. A comparison to a previously developed radar-based precision takeoff and landing system is carried out.

Keywords

Precision Landing; Thermal imaging; Radar Altimeter; Thermal Marker

1. INTRODUCTION

Research on Vertical Take Off and Landing Systems (VTOLS) has shown huge potential in various fields of application. Examples are the delivery of parcels [1, 2] or medication [3, 4], the application for surveillance and search and rescue [1, 5], remote sensing of vegetation [6] or the transformation of the mobility of people [7, 8]. Autonomous operation is already widely possible relying on the Global Navigation Satellite System (GNSS). During takeoff and landing, however, relying on GNSS only yields limitations regarding availability and safety. GNSS is in particular close to the ground susceptible to spoofing and jamming. Structure close to the landing area like buildings or urban canyons can cause errors due to multipath or shading. Safe and reliable operation has to be ensured even in bad visual conditions like darkness, direct sunlight, fog or smoke.

This paper presents a precision takeoff and landing system based on thermal imaging and radar. Both sensors can operate even in bad visual conditions. The system consists of a landing platform with thermal markers which are implemented with Peltier modules. A thermal camera is attached to the VTOL facing towards the ground. Detection of the thermal markers enables pose estimation which is the key to our precision takeoff and landing approach. Even though thermal cameras are expensive sensors, they are widely used e.g. for remote sensing of vegetation [6] surveillance or search and rescue [5]. Thus, using them for precision takeoff and landing does not necessarily imply an additional sensor which adds weight and cost.

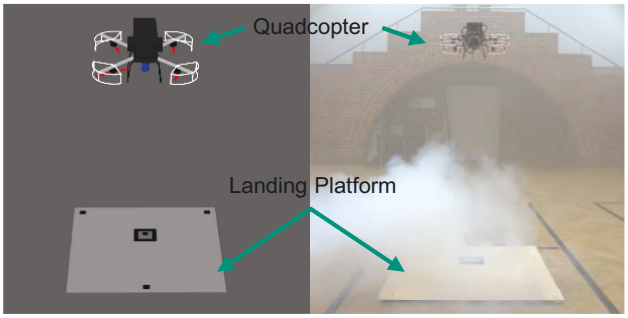

FIG. 1. Proposed system: Snapshot of the simulation (left) and a real test flight with bad visual conditions (right). The proposed system enables safe and reliable takeoff and landing even in bad visual conditions.

Our contributions are:

- A robust precision takeoff and landing system based on a thermal camera and a radar altimeter which can be used even on small VTOLs.
- A design of a landing platform consisting of thermal markers suitable for precision takeoff and landing.
- A robust and real time capable detection algorithm for the landing platform.

The remainder of the paper is structured as follows. The flight scenario is described at first, followed by related work on precision takeoff and landing. Next, the proposed precision takeoff and landing with thermal imaging is presented. Finally, results from simulation, test flights and a comparison to a previously developed radar based precision takeoff and landing system are given.

doi:10.25967/530121

The following conventions are used in this paper. Vectors are printed as bold lower case letters (e.g. $\mathbf{p}$), matrices as bold upper case letters (e.g. $\mathbf{R}$), scalars as non bold letters (e.g. m) and constants as upper case non bold letters (e.g. L). A vector in the global frame (navigation-frame) is $\mathbf{p}^n$ and the rotation matrix from the body frame into the n-frame is $\mathbf{C}_b^n$.

2. SCENARIO

This section summarizes the scenario which integrates our proposed system into autonomous flights of VTOLs. A typical VTOL flight consists of the three phases takeoff, mission and landing.
The mission depends on the use case. Urban air mobility, parcel delivery or search and rescue missions are some examples. These missions can be carried out autonomously relying on GNSS. We assume, that during mission, a certain height is kept such that typical GNSS errors can be neglected.
For takeoff and landing, an accurate control of the horizontal position is required such that the VTOL keeps centered above the center of the landing platform. This is called precision takeoff and landing. During takeoff and landing, a different navigation technique is required as GNSS is not reliable during these flight phases. In particular, close to the landing area, threats due to spoofing and jamming are present. In addition, errors caused by multi path or shading due to buildings or urban canyons further degrades the GNSS position accuracy. Thus, a GNSS denied navigation technique is required.
To enable safe and reliable operation even in bad visual conditions, we propose a thermal camera based navigation. This system provides an accurate localization which is suitable for precision takeoff and landing. A visualization of the whole flight scenario is given in Fig. 2. The takeoff and landing height is considered to be $15\,\mathrm{m}$ within this paper.

3. RELATED WORK

Precision takeoff and landing is an active field of research. It is summarized and evaluated in the following. Precision landing based on high precision GNSS like Real Time Kinematic (RTK) has been showed e.g. in [9]. High accuracy GNSS based navigation which does not need custom ground stations, like Precise Point Positioning (PPP) [10] is also widely applied even in commercial products. Due limited safety and availability during takeoff and landing, such systems do not fulfill our requirements.
Technology from general aviation which does not rely on GNSS like the Instrument Landing System (ILS) or Microwave Landing System (MLS) cannot be used for our VTOL use case due to cost, size and weight of the required components onboard of the VTOL and

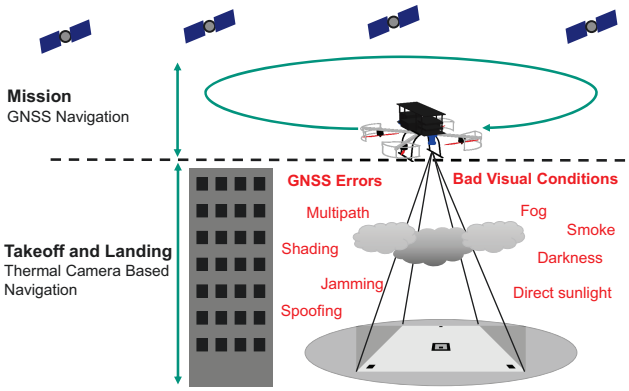

FIG. 2. Flight scenario: Takeoff, mission and landing. Thermal camera based navigation is applied during takeoff and landing.

on the ground. Although, the MLS has been evaluated for the application on helipads for conventional helicopters in [11], required space on the ground is unrealistic for urban environments and especially for the landing areas of small VTOLs.
A solution is to apply visual navigation techniques [12–14]. Typically, visual markers placed on the landing platform are detected with a down facing camera. Many different types of visual marker have been developed. Popular examples based on squared markers are AprilTag [15] and AruCo [16]. Circular patterns are for example proposed by [17]. To enable operation also during night, [12] proposed to illuminate the visual markers. Precision landing with visual marker in clear sight proved to be accurate and reliable. Bad visual conditions like fog or smoke, however, renders vision based approaches infeasible.
Approaches based on radar or Ultra Wideband (UWB) also proved to be suitable for precision landing [18–22]. These approaches are based on radio frequencies that are less affected by bad visual condition as compared to the visual spectrum. Systems based on UWB apply runtime measurements between each UWB tag. Thus, localization can be carried out [18, 21]. For precision landing, a huge area has to be covered with UWB tags to achieve good localization accuracies [19]. Therefore, [20] proposed to combine a single range measurement with and Angle of Arrival (AoA) measurement. Thus, only a single tag is required on the ground. Recently, we proposed to use only passive radar reflectors on the ground [22]. This system will be compared with the proposed, thermal based system at the end of this paper.
Advances in thermal imaging achieved light weight sensors which can be integrated even on a small VTOL (takeoff weight $< 2\,\mathrm{kg}$). Thermal imaging offers the possibility to apply state of the art image processing algorithms. In addition, bad visual conditions do not affect thermal imaging strongly. The authors of [23] presented thermal markers. These are cre-

ated using space heaters with an overlaying mask structure. Building upon visual marker detection, thermal markers have been developed and their applicability in bad visual conditions demonstrated. Our approach, however, implements thermal marker with low cost and low power Peltier modules. We combine an ArUco marker with blob-like features for a robust detection of the landing platform.

4. PRECISION TAKEOFF AND LANDING WITH THERMAL IMAGING

4.1. Thermal Marker

In contrast to visual cameras, thermal imaging is not affected by challenging visual conditions. Thermal imaging offers the ability to deal with DVEs like fog. An experiment is given in Fig. 3. The top row shows the visual images and the bottom row the thermal images. On the left good visual and on the right bad visual conditions are present. The marker detection of the thermal image is not affected by the fog shown by the blue square in Fig. 3.

Marker detection with visual cameras has been well researched. The application of fiducial markers like ArUco [16], AprilTag [15] is well established. These approaches encodes an ID into the marker. Assuming that each marker ID exists only once in the environment, fiducial marker detection solves the association problem. Detection of fiducial markers however, is computationally demanding which implies a high load on embedded platforms. Thus, more light weight markers based on circular patterns like WhyCon [17] or blobs [24] has been proposed. Since additional information, like IDs cannot be encoded in such markers, a more sophisticated association is required.

Due to the processing speed, robustness and integration into state of the art computer vision frameworks like OpenCV [24], ArUco [16] is evaluated in more detail. We observed different detection properties within the individual markers from the marker dictionary. Therefore, the most stable detectable marker id has been determined in experiments. Next, the maximum detection range depending on the marker size has been evaluated with the previously determined marker. This has been done using a visual camera with the same resolution and comparable Field of View (FOV) as the thermal camera. A final test of the same marker size using visual and thermal images showed the same results. Thus, the same properties for visual and thermal marker detections can be assumed for the thermal AruCo marker in this case. An analysis of the detection range experiments is given in Tab. 1 using a camera with 640×512 pixels resolution.

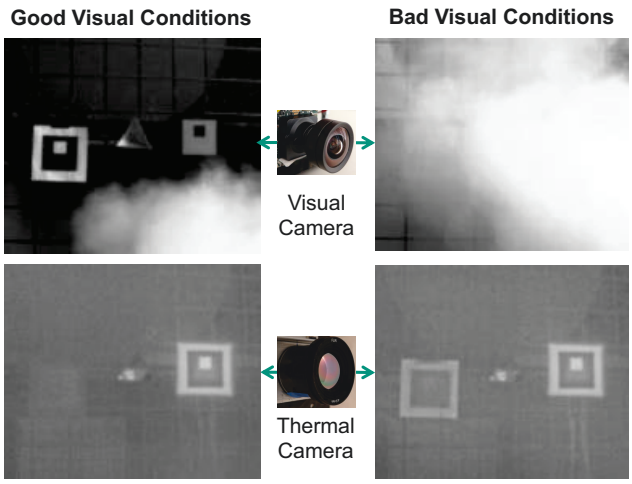

FIG. 3. Visual (top) and thermal (bottom) image with good (left) and bad (right) visual conditions. Thermal images are not affected by the fog.

Marker Size	Maximum Detection Range
$10\,\mathrm{cm}$	$4-5\,\mathrm{m}$
$15\,\mathrm{cm}$	$7-8\,\mathrm{m}$
$20\,\mathrm{cm}$	$9-10\,\mathrm{m}$
$25\,\mathrm{cm}$	$11-12\,\mathrm{m}$

TAB. 1. ArUco marker: Marker size versus detection range analysis.

We opted for easy manufacturing of the thermal markers. Thus, more complex markers like AprilTag or WhyCon were neglected. Instead, the best detectable ArUco marker and blob marker are selected. The thermal markers are build with Peltier modules. These create a temperature difference between their upper and lower side. A heat sink is placed on the cool side and the warm side is left free (blob) or connected to an aluminum plate (ArUco). The aluminum plate is coated with a non reflective material. An mask is placed in short distance on top the plate at the ArUco marker to provide a temperature contrast. Since the Peltier modules forces temperature difference, markers are clearly visible in thermal images independent of the ambient temperature.

4.2. Landing Platform

Goal of the landing platform design is to enable a detection up to $15\,\mathrm{m}$. Using ArUco markers only would require large markers with a size above $25\,\mathrm{cm}$. Since the markers need to be heated, they have to be as small as possible to conserve energy. Using blob markers only enables the required detection height. Advanced marker association would, however, be required. This would be difficult during takeoff as only a single marker is visible due to the close proximity to the landing target.

Therefore, we use a single ArUco marker with three blob markers to combine the complementary characteristics of both marker types. The ArUco marker has

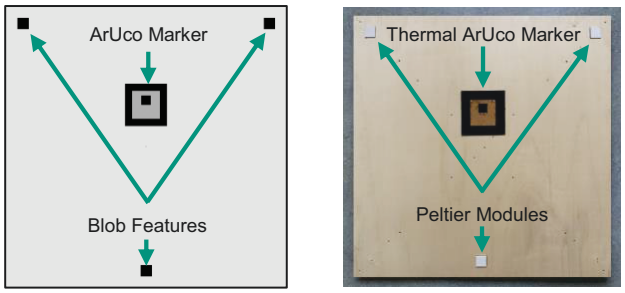

FIG. 4. Landing platform used for simulation (left) and demonstrator for test flights (right).

a edge length of $10\,\mathrm{cm}$ and the squared blob markers of $4\,\mathrm{cm}$. Fig. 4 shows the landing platform used for simulation on the left and the landing platform prototype for test flights on the right. The ArUco marker is placed a little above the center. That way, it will be in the FOV of the thermal camera if the quadcopter is placed in the center of the landing platform. The landing platform is $1\,\mathrm{m} \times 1\,\mathrm{m}$. Low power was required during our flight experiments, $10\,\mathrm{W}$ total turned out to be sufficient to enable robust detection.

4.3. Landing Platform Detection

Depending on the height above the landing platform different detection modes are applied:

- At low altitudes ($h < 1\,\mathrm{m}$), only the ArUco detection will be done as the blob markers are not in the FOV of the thermal camera.
- At mid range altitudes ($1\,\mathrm{m} \leq h < 4\,\mathrm{m}$) the ArUco detector and the blob detector will be run.
- At high altitudes ($h \geq 4\,\mathrm{m}$) only the blob detector will be executed as an ArUco detection will fail at these altitudes.

Three examples for each detection interval are depicted in Fig. 6. Since the height is assumed to be measured by the radar altimeter, the detection interval can be determined online.
An advanced detection algorithm does not need to be applied if in AruCo only detection mode. Known image points to world points association is given in this case, since this information in encoded in ArUco markers. The detection strategy for the two other detection modes will be explained in the following
The detection algorithm assumes that the landing platform is approximately gravity aligned. Furthermore, the height above the landing platform has to be approximately provided. Using the radar altimeter worked good in our case. The final input is the roll angle θ_b^n and pitch angle ϕ_b^n of the VTOL. Both angles are provided by the onboard flight controller since both are vital for the attitude control.
The detection is done in various steps. At first all image points from blobs and, if available, the mean of

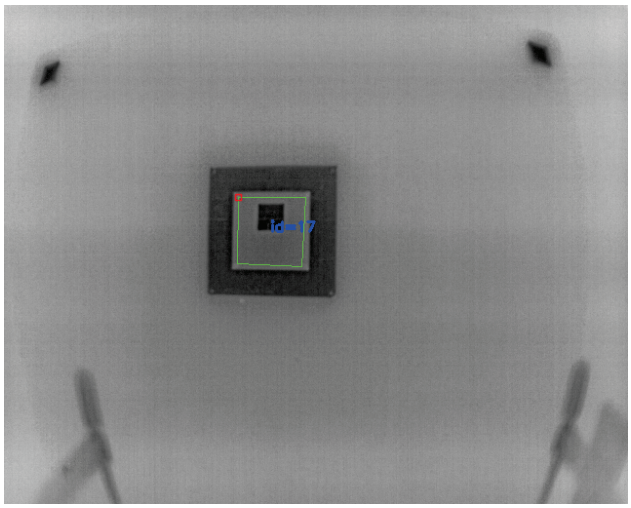

(a) Height: 0.5m, ArUco only

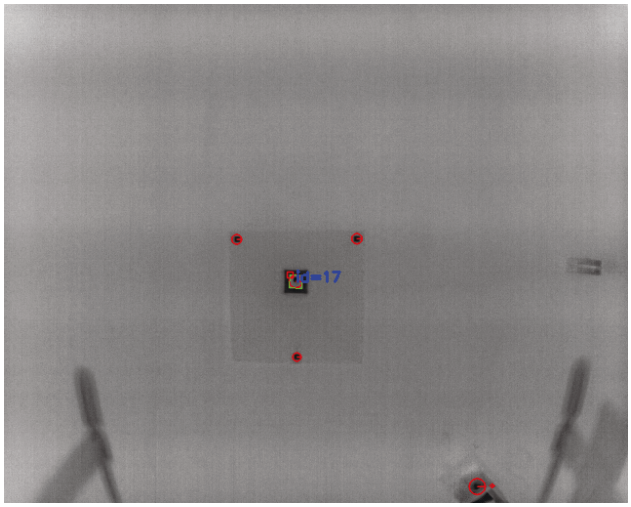

(b) Height: 3m, ArUco and Blobs

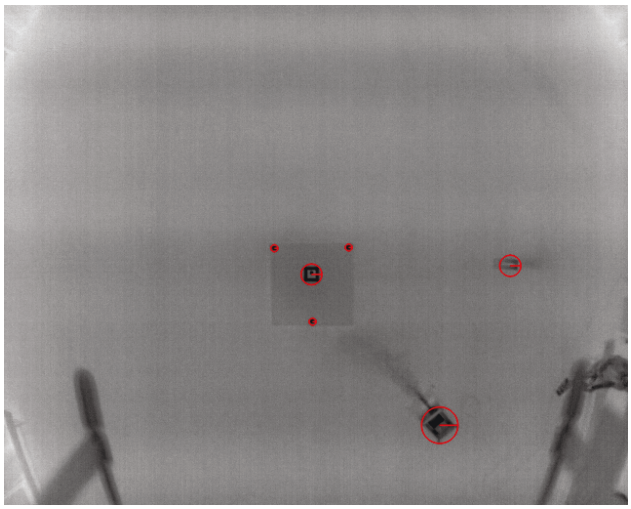

(c) Height: 5m, Blobs only

FIG. 5. Visualization of the three different landing platform detection modes.

the ArUco marker corners are transformed into the gravity aligned body frame or stabilized frame $\{\}^s$. Defining the intrinsic camera matrix $\mathbf{K}$ as:

$$\mathbf{K} = \begin{bmatrix} f_x & 0 & c_x \\ 0 & f_y & c_y \\ 0 & 0 & 1 \end{bmatrix} \tag{1}$$

with the focal length f_x and f_y and the principal point c_x and c_y enables the projection of a point from image coordinates $\mathbf{p}^{\mathrm{px}} = [u, v]$ into homogenous camera coordinates $\tilde{\mathbf{p}}^{\mathrm{c}*}$ by:

$$\tilde{\mathbf{p}}^{\mathrm{c}*} = \mathbf{K}^{-1} \begin{bmatrix} u \\ v \\ 1 \end{bmatrix}. \tag{2}$$

Next lens distortions are removed which results in undistorted, homogenous camera coordinates $\mathbf{p}^{\mathrm{c}*}$. Assuming that the z-axis of the thermal camera and radar altimeter coincides enables to calculate the projected point in the camera frame $\{\}^c$:

$$\mathbf{p}^c = h_z \mathbf{p}^{\mathrm{c}*} \tag{3}$$

with the z-component h_z of the ground target measured by the radar altimeter. Using the global roll angle θ_b^n and pitch angle ϕ_b^n of the VTOL enables to state the rotation matrix $\mathbf{C}_b^s$ from the body frame $\{\}^b$ to the stabilized frame $\{\}^s$. Transformation of the projected point into the stabilized frame using a previously calibrated body frame to thermal camera frame rotation matrix $\mathbf{C}_c^b$ yields:

$$\mathbf{p}^s = \mathbf{C}_b^s \mathbf{C}_c^b \mathbf{p}^c. \tag{4}$$

This is done for all detected image points which results in Cartesian coordinates. The geometric matching relies only on the x and y coordinate. Goal is to determine the center and to associate the other three blobs to their ID as depicted in Fig. 6. The association is achieved using a geometric matching based on the distances d_0, d_1, d_2 and angles $\alpha_{01}, \alpha_{02}, \alpha_{12}$ of the surrounding blobs to the center. The light green area in Fig. 6 shows the search area during the matching. The association, that matches best regarding distance and angle is assumed to be correct one. Based on the association, the pose estimation is performed as described in the next section.

4.4. Pose Estimation

The aim of the our approach is to integrate our thermal based precision takeoff and landing with state of the art flight controllers. Thus, a loosely coupling of the image based pose estimation and the navigation filter of the flight controller is implemented. Based on the landing platform detection, an image based pose estimation is done. This pose estimate is then fused

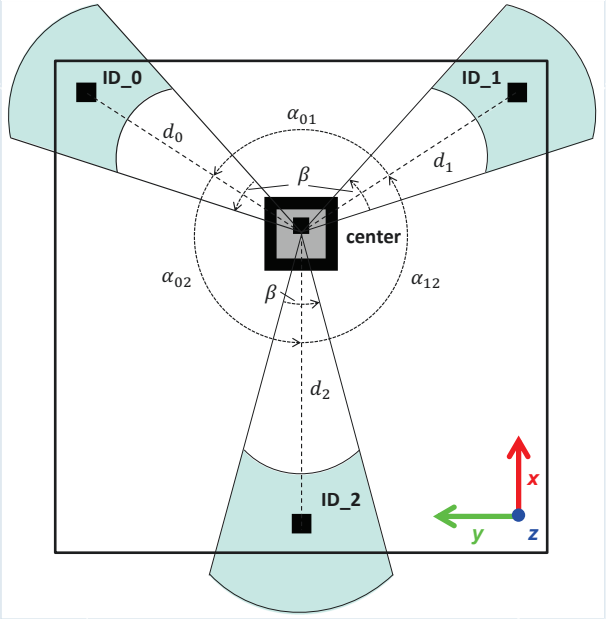

FIG. 6. Landing platform detector: Detection is based on geometric matching whereas the light green areas are used as search space for the outer blobs.

with an Extended Kalman Filter whereas an outlier rejection is carried out as well. This architecture enables easy integration with state of the art flight controllers e.g. Pixhawk [25] as used in our work. In addition, the application of low cost IMUs is proved. Two approaches regarding pose estimation are explored:

- Pose estimation based on the so called Perspective-n-Point-problem (PnP) [26].
- Position and yaw estimation aided by IMU and radar altimeter.

Pose estimation with PnP is a well established method for image based pose estimation which has a good support in state of the art image processing frameworks like OpenCV [24]. Given at least three image point to world point correspondences along with the camera calibration enables to solve the PnP-problem. This results in the 6-DoF pose of the landing platform which minimizes the reprojection error. Main disadvantage of this method is, however, the requirement for very exact image point coordinates. Even small displacements yields in particular in difficult perspectives huge pose estimation errors. These difficult perspectives are quite common in our use case. All features are placed on the $1\,\mathrm{m} \times 1\,\mathrm{m}$ landing platform. At larger altitudes, e.g. $> 3\,\mathrm{m}$, all features are located at a quite small area of the image. Thus, pose estimation based on PnP will degrade. Therefore, the application of another localization method is presented. The main idea of the IMU and radar altimeter aided method is make use of these sensors. Since we want to determine only the position and yaw angle,

the pose estimation can be simplified. This approach uses the projected detections in the stabilized frame $\mathbf{p}^s$ from (4). Based on this, a similar approach of pose estimation as proposed in [22] can be applied. At first the yaw angle of the VTOL is estimated, then the estimation of the position is done. The angles of the vector connecting the outer blobs with the center is calculated by:

$$\hat{\psi}_{c0} = \operatorname{atan2}(\mathbf{p}^s_{0,y} - \mathbf{p}^s_{\text{center},y}, \mathbf{p}^s_{0,x} - \mathbf{p}^s_{\text{center},x}), \tag{5}$$

$$\hat{\psi}_{c1} = \operatorname{atan2}(\mathbf{p}^s_{1,y} - \mathbf{p}^s_{\text{center},y}, \mathbf{p}^s_{1,x} - \mathbf{p}^s_{\text{center},x}), \tag{6}$$

$$\hat{\psi}_{c2} = \operatorname{atan2}(\mathbf{p}^s_{2,y} - \mathbf{p}^s_{\text{center},y}, \mathbf{p}^s_{2,x} - \mathbf{p}^s_{\text{center},x}). \tag{7}$$

Applying (5) - (7) using the real landing platform prototype yields the true angles $\psi_{c0}, \psi_{c1}, \psi_{c2}$. Assuming alignment of the landing platform with the global x- and y-axis yields the estimated yaw angle $\hat{\psi}^n_b$ of the VTOL:

$$\hat{\psi}^b_b = \frac{1}{3}\sum_{i=0}^{2} \hat{\psi}_{ci} - \psi_{ci}. \tag{8}$$

The rotation matrix from the body frame to the global navigation frame $\mathbf{C}^n_b$ is calculated using the global roll angle θ^n_b, the pitch angle ϕ^n_b of the VTOL and the global yaw angle ψ^n_b from (4). Thus, each detected point can be transformed into the global frame:

$$\hat{\mathbf{p}}^n_{\{0,1,2,c\}} = \mathbf{C}^n_b \mathbf{C}^b_c \mathbf{p}^c_{\{0,1,2,c\}}. \tag{9}$$

The mean of all detection residuals yield the estimated global position $\hat{\mathbf{p}}^n_b$:

$$\hat{\mathbf{p}}^n_b = \frac{1}{4}\sum_{i\in\{0,1,2,c\}} \hat{\mathbf{p}}^n_i - \mathbf{p}^n_i. \tag{10}$$

The estimated global position $\hat{\mathbf{p}}^n_b$ and yaw angle $\hat{\psi}^n_b$ are fused with the data of an IMU in an Extended Kalman Filter. The measurement is, however, only fused if it passed an outlier test. Result is a smooth localization at high rate. Even short outages of the thermal camera based motion estimation are bridged using this kind of sensor fusion.

4.5. Guidance

The guidance manages the takeoff and landing of the VTOL. During takeoff the horizontal position is controlled such that the VTOL stays centered above landing platform. In our test flights, we applied a maximum vertical velocity of $1\,\mathrm{m/s}$. The position controller is a cascaded PID controller implemented as part of the Pixhawk flight controller. The landing guidance operates in two modes: Approach and touch down. In the approach phase, a maximum vertical velocity of $1\,\mathrm{m/s}$ is applied while the horizontal position is kept centered above the landing platform. As soon as the VTOL gets close to the landing platform (height $< 1\,\mathrm{m}$), a refinement phase is executed. The VTOL hovers until the horizontal position is sufficient close the center of the platform. In addition, the horizontal velocity must be close to zero. If both conditions are met, the final touch down is performed.

5. EXPERIMENTAL RESULTS

The proposed system has been evaluated in simulation and real test flights. The real test flights have been done in a motion capture system for accuracy evaluation and in a gym with bad visual conditions which were created with a fog machine.

5.1. Quadcopter

The quadcopter prototype shown in Fig. 7 has been used for the test flights. The motors are mounted facing downward. The quadcopter has a diameter of $55\,\mathrm{cm}$ and a takeoff weight below $2\,\mathrm{kg}$. Fig. 7 shows the thermal camera and radar altimeter. A FLIR Boson 640 thermal camera with a resolution of 640×512 pixels and a TI IWR1443Boost EVM radar are used. The thermal images are processed with $10\,\mathrm{Fps}$ and the radar altimeter is running at $20\,\mathrm{Hz}$. All processing is done onboard on a credit card size UpCore embedded computer. A Pixhawk [25] flight controller is used. ROS [27] is widely used for communication and as base framework.

5.2. Simulation

The system has been evaluated in simulation. A realistic simulation setup is used based on Gazebo. The software in the loop mode of Pixhawk is applied such that the same flight controller code is executed for both simulation and real flights. Sensor noise was simulated with values observed on real test flights. A snapshot of the simulation along with example images and detector visualization is given in Fig. 8.

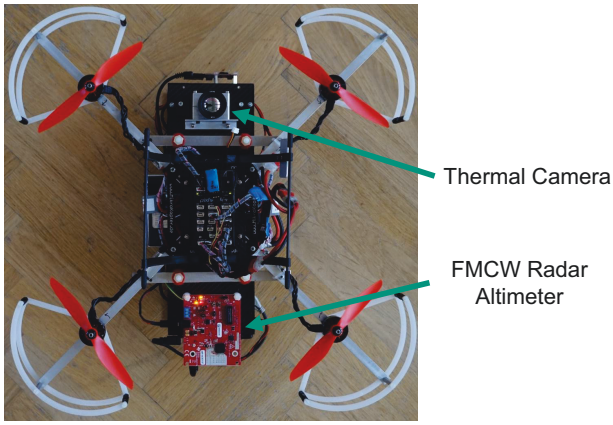

FIG. 7. Bottom view of the VTOL used for the test flights: Quadcopter with $< 2\,\mathrm{kg}$ takeoff weight.

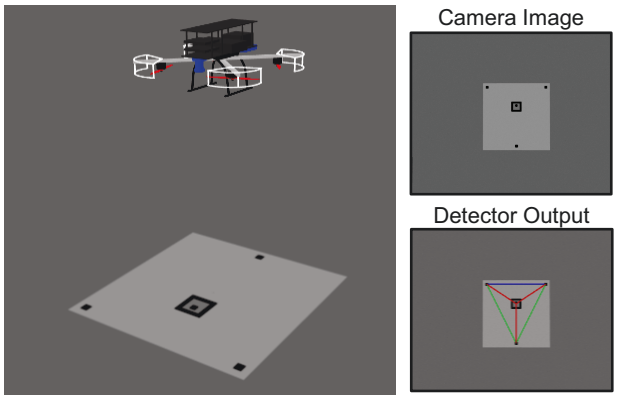

FIG. 8. Snapshot from the simulation (left) with the corresponding simulated image (right, top) and the output of the landing platform detector (right, bottom).

The images of the thermal camera have been simulated with a gray scale camera model. The same FOV and image size has been used. Fig. 9 shows an example of a simulated image on the left and a thermal image from one of the test flights on the right. The landing platform looks quite similar, despite more noise and non uniformity of the thermal image. Detection of the landing platform was in fact better with real thermal images. Based on thermal images, detection of the landing platform worked even at a distance of $15\,\mathrm{m}$. Due to the heat of the Peltier modules, they appear very clear, even from far distance. In simulation, however, the maximum detection range is circa $10\,\mathrm{m}$. This can be explained by the fact that only a passive structure is simulated, which does not act as a light source.

Two different types of pose estimation has been presented in Sec. 4.4. They have been evaluated in our first simulation experiment. A takeoff and landing are executed. During takeoff, a stepwise height profile is flown for better evaluation. The step size is $1\,\mathrm{m}$ and changed every $3\,\mathrm{s}$ with a maximum at $9\,\mathrm{m}$. The resulting ground truth height is shown in the upper plot of Fig. 10a. The errors of the PnP based and IMU based pose estimation are analyzed in the lower three plots of Fig. 10a. At low altitudes (below $4\,\mathrm{m}$) this method turns out to be quite accurate.

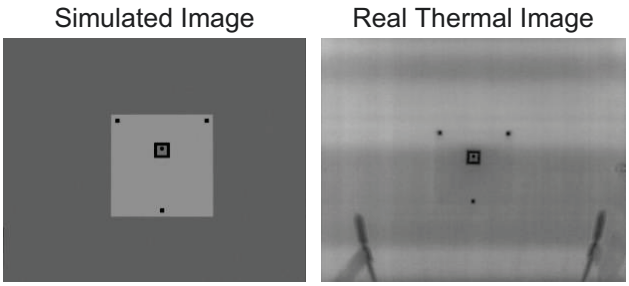

FIG. 9. Simulated image (left) and real thermal image from test flights (right).

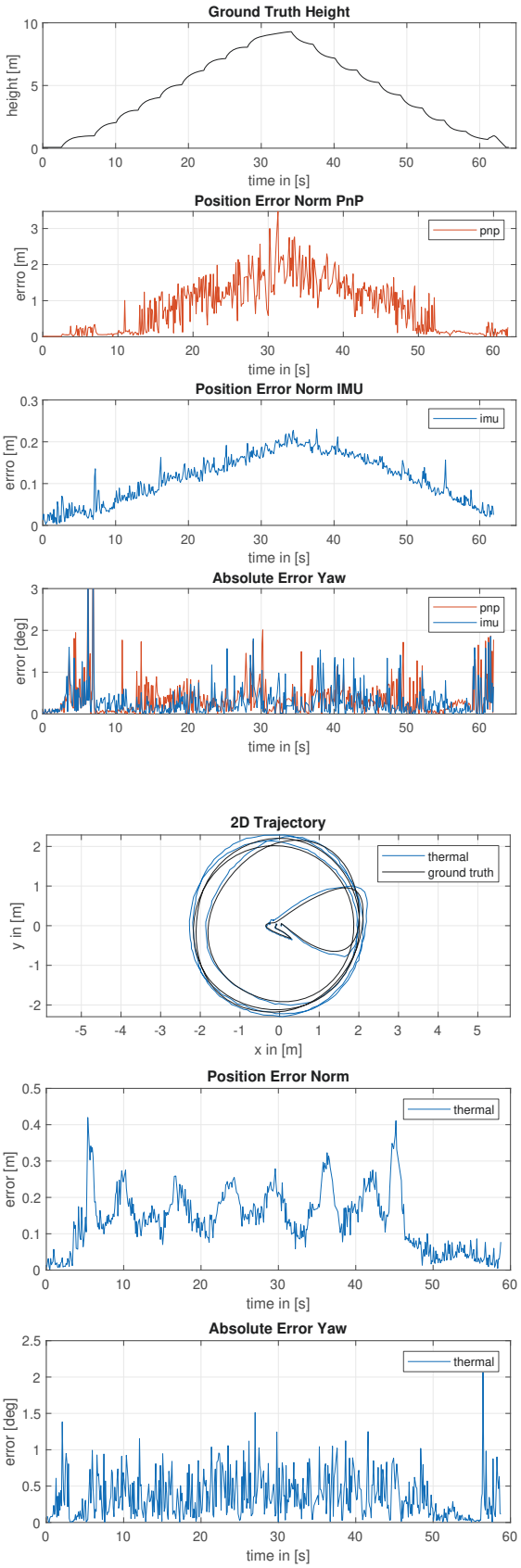

(b) Circular trajectory 8m height

FIG. 10. Evaluation of the two simulation results: Pose estimation (top) and circle flight (bottom).

At higher altitudes, however, the perspective gets difficult for the PnP based pose estimation since the distance between the blobs gets small. The IMU based method on the other hand shows small errors which are proportional to the altitude. This method depends on accurate roll and pitch angles. Due to offsets of the accelerometers, roll and pitch also shows small offsets. Thus, the position error grows with larger altitudes. The position error norm of the IMU based pose estimation is circa by a factor of 10 smaller than the PnP based method at higher altitudes.

The yaw error is similar for both methods and shows little dependency on the altitude. Below $1\,\mathrm{m}$ (around $6\,\mathrm{s}$ and $60\,\mathrm{s}$), however, larger yaw errors can be observed. Only the ArUco marker is detected which results in a less accurate yaw estimation.

The second simulation flight experiment evaluates the the accuracy and detection performance at more challenging conditions. Therefore, a circular flight a $8\,\mathrm{m}$ was simulated. The ground truth along with the IMU based pose estimation are at the top of Fig. 10b During the circle phase, yaw was always controlled such that the quadcopter pointed forward. Thus, yaw covered values for full $360\,^\circ$ at an altitude close to the maximum detection height. Successful pose estimation with position norm errors below $0.4\,\mathrm{m}$ (mean $0.13\,\mathrm{m}$) and absolute yaw errors below $2\,^\circ$ (mean $0.35\,^\circ$) prove the robustness of the detector and the accuracy of the IMU based pose estimation.

5.3. Motion Capture Test Flight

The accuracy of the thermal based pose estimation has been evaluated using a motion capture system. A snapshot of the flight is shown in Fig. 11. During these flights, the height has been varied between $0.5\,\mathrm{m}$ and $2\,\mathrm{m}$ above the landing platform. Ground truth is provided by a motion capture system. In particular close to the landing platform, a high accuracy localization is crucial for a precise landing.

The thermal based pose estimation is evaluated regarding the position error norm and the absolute yaw error. This is done for both pose estimation approaches from section 4.4 similar to our first simulation experiment. Fig. 12 shows the result for a $30\,\mathrm{s}$ test flight. The mean absolute errors for both pose estimation techniques are summarized in Tab. 2.

Both flights have a mean position error norm of circa $0.05\,\mathrm{m}$. Both approaches yield a high accuracy position estimation as shown be the small errors. PnP tends to more susceptible towards image noise. This can be observed around $5\,\mathrm{s}$, $18\,\mathrm{s}$ and $26\,\mathrm{s}$. At these timestamps, the height was below $1\,\mathrm{m}$. Thus, only the ArUco marker was detected which covers only a small area of the image. Consequently, the PnP method shows a high frequency noise error. The position error of the IMU based approach is not affected by this

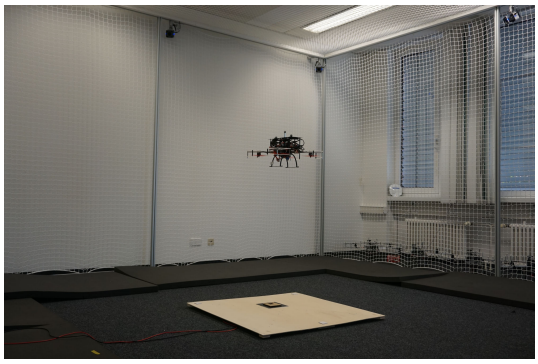

FIG. 11. Snapshot of motion capture test flight.

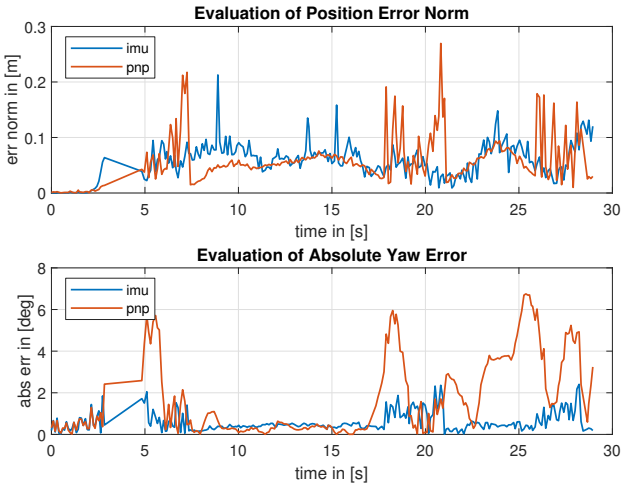

FIG. 12. Accuracy analysis.

	e_x	e_x	e_x	e_ψ
PnP	$0.05\,\mathrm{m}$	$0.02\,\mathrm{m}$	$0.01\,\mathrm{m}$	$1.67\,^\circ$
IMU	$0.02\,\mathrm{m}$	$0.03\,\mathrm{m}$	$0.03\,\mathrm{m}$	$0.59\,^\circ$

TAB. 2. Mean absolute errors motion capture.

phenomenon. Similar position errors have been observed in simulation, see e.g. the first $10\,\mathrm{s}$ in Fig. 10a, which corresponds to a max height of $2\,\mathrm{m}$.

The mean absolute yaw error is circa $1.7\,^\circ$ for the PnP approach and circa $0.6\,^\circ$ for the IMU based approach. The PnP based yaw estimation has a larger mean error and also some outliers e.g. at $24\,\mathrm{s}$. Both methods show accurate yaw estimation once the whole landing platform is in the FOV and all blobs are used for pose estimation. In this case, the distance of the detections in the image is quite large. Thus, detection errors in the magnitude of a few pixels does not affect the accuracy strongly.

5.4. Indoor Test Flights

Demonstration of the thermal based precision takeoff and landing system has been done indoors in a gym. No localization other than the thermal based pose estimation method IMU has been used. All flights were

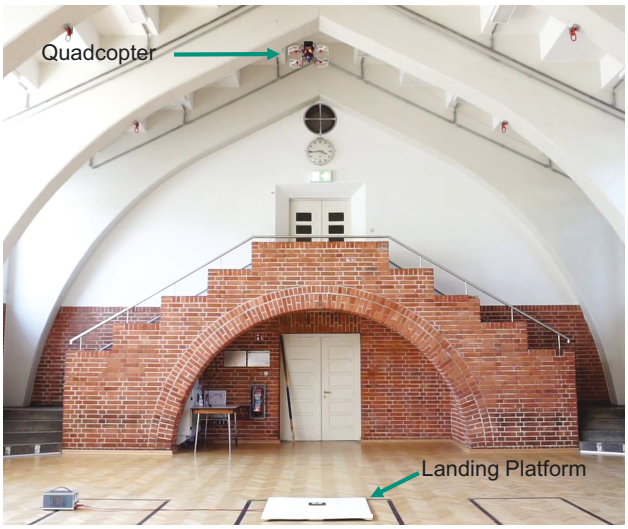

(a) Flight at good visual conditions.

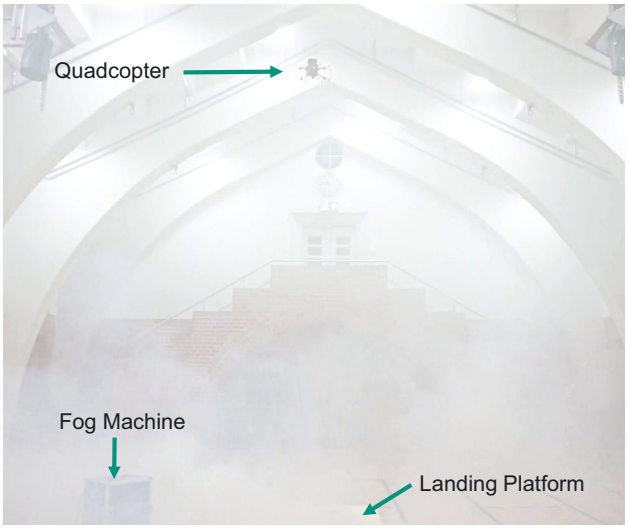

(b) Flight at bad visual conditions.

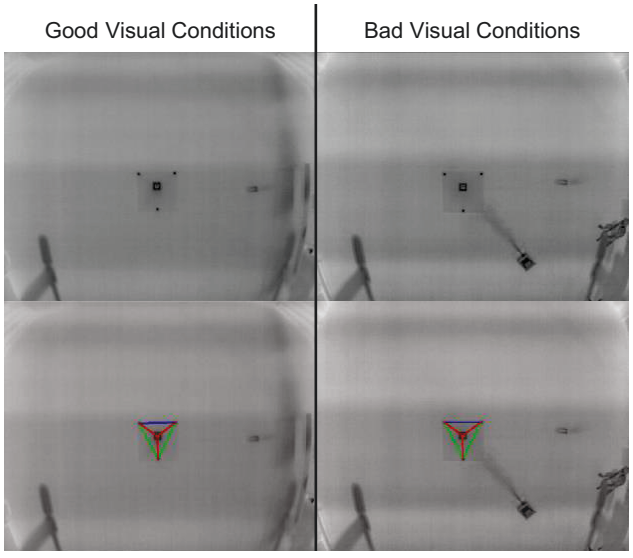

(c) Onboard views of the thermal camera.

FIG. 13. Summary indoor test flights at 5m.

conducted completely autonomously using the guidance from Sec. 4.5. Bad visual conditions have been simulated with a fog machine. A snapshot of a test flight with good visual conditions is shown in Fig. 13a and of bad visual conditions in Fig. 13b. Both snapshots are at $5\,\mathrm{m}$ above the landing platform which was the maximum flight height of this environment. The onboard view for both flights is shown in Fig. 13c. The proposed system was not affected by the fog proving it being suitable for degraded visual environments. All 10 test flights up to different altitudes ($2\,\mathrm{m}$-$5\,\mathrm{m}$) has been successful with a touch down close to the center of the landing platform.

5.5. Maximum Detection Range

Due to the limited maximum flight height at the gym test site, a different experiment has been conducted in one of our labs to evaluate the maximum detection distance. The landing platform has been placed on one side of the room. Due to furniture and reflections, several blobs were detected as shown in Fig. 14a. Robust detection of the landing platform was possible up to a range of $15\,\mathrm{m}$ as shown in Fig. 14b.

5.6. Comparison to Radar based System

This section compares the proposed thermal based precision landing system with previously proposed radar based system [22]. The main components are shown in Fig. 15. Only the FMCW radar is used as main sensor. It detect passive radar reflectors placed below the landing platform which enables pose estimation. The global pose estimates are also fused with an EKF with outlier rejection. A summary of the comparison is given in Tab. 3.
Both systems has been demonstrated in bad visual conditions successfully. The same landing platform size is used for a better comparison. We chose $1\,\mathrm{m} \times 1\,\mathrm{m}$ for the demonstrators. The ground unit or equipment needed for the landing platform is different. The radar based system requires only passive reflectors. The thermal based system, however, needs active Peltier modules for heating. Both systems has been evaluated in similar flight experiments with motion capture in close proximity of the landing platform ($< 2\,\mathrm{m}$ above the landing platform). The radar based system achieved an mean position error norm of $0.07\,\mathrm{m}$ [22]; the thermal based system $0.05\,\mathrm{m}$. Thus, the position accuracy in close proximity is very accurate. The yaw error is more different. The radar based system achieved a mean absolute yaw error of $4\,^\circ$ whereas the thermal based system achieved $0.6\,^\circ$. The thermal based system showed a more accurate pose estimation also during the test flights which resulted in more stable hover positions. The detection range of the landing platform enables a detection up to $5\,\mathrm{m}$ for radar and $15\,\mathrm{m}$ for thermal.

(a) Blob detections at 15m distance.

(b) Landing platform detection at 15m distance.

FIG. 14. Maximum detection range landing platform.

Both systems are running in real time on a credit card size embedded platform like the UpCore. The CPU usage is low for radar whereas it is high for thermal due to the image processing. Thus, the pose estimation rate of the thermal system is limited to $10\,\mathrm{Hz}$. Since a standard FMCW radar sensor is used, it is of low cost in particular compared to a thermal camera. The total weight of both systems is below $150\,\mathrm{g}$ even for the thermal system. Consequently, both systems can be applied even on small VTOLs like our quadcopter (takeoff weight $< 2\,\mathrm{kg}$ and $55\,\mathrm{cm}$ diameter).

Thus, the thermal camera based system provides higher accuracies and longer detection ranges at the cost of higher computational load and the requirement of an active landing platform with Peltier modules. The radar based system is low cost, requires only little CPU usage and only passive radar reflectors. However, it provides a lower maximum detection range and is less accurate.

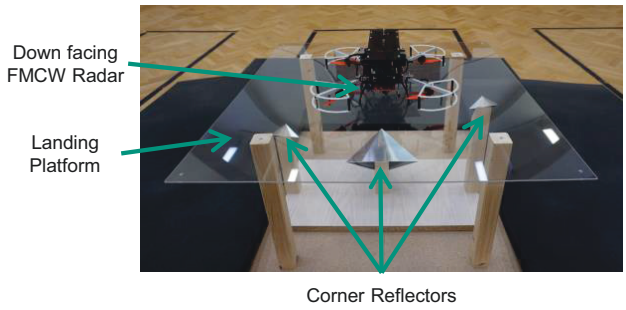

FIG. 15. Radar based system [22].

	Radar	Thermal
Bad Visual Conditions	yes	yes
Size Landing Platform	$1\,\mathrm{m} \times 1\,\mathrm{m}$	$1\,\mathrm{m} \times 1\,\mathrm{m}$
Ground unit	passive	active
Position Accuracy	good	very good
Yaw Accuracy	medium	very good
Detection range	ca. $5\,\mathrm{m}$	ca. $15\,\mathrm{m}$
Embedded Realtime	yes	yes
CPU Usage	low	high
Max Rate	$20\,\mathrm{Hz}$	$10\,\mathrm{Hz}$
Sensor cost	low	high
Total weight	$50\,\mathrm{g}$	$50\,\mathrm{g} + 80\,\mathrm{g}$

TAB. 3. Comparison of precision takeoff and landing systems: Radar based vs. thermal based.

6. CONCLUSION

This paper presented an autonomous precision takeoff and landing system for VTOLs that can operate in GNSS denied and degraded visual environments. Relying on thermal imaging and a radar altimeter enables safe and reliable guidance during takeoff and landing. The proposed system uses a down facing thermal camera to detect the landing platform which is built with thermal makers. Inspired by visual markers, a combination of different makers is proposed and a robust detection algorithm developed.

Our approach is tested in simulation and with real test flights. The accuracy close to the landing platform has been evaluated with test flights in a motion capture system. Demonstrations with indoor test flights proved the proposed system for precision takeoff and landing even in bad visual conditions. A comparison to a previously developed radar based precision takeoff and landing system showed the advantages and disadvantages of both approaches.

Integration and test flights with GNSS based missions will be evaluated in future work.

Contact

christopher.doer@kit.edu

References

[1] A. Otto, N. Agatz, J. Campbell, B. Golden, and E. Pesch, "Optimization approaches for civil applications of unmanned aerial vehicles (uavs) or aerial drones: A survey," *Networks*, vol. 72, no. 4, pp. 411–458, 2018.

[2] A. Goodchild and J. Toy, "Delivery by drone: An evaluation of unmanned aerial vehicle technology in reducing co2 emissions in the delivery service industry," *Transportation Research Part D: Transport and Environment*, vol. 61, pp. 58 – 67, 2018.

[3] J. E. Scott and C. Scott, "Drone delivery models for healthcare," in *2017 Hawaii International Conference on System Sciences (HICSS)*, 2017.

[4] J. C. Rosser, V. Vignesh, B. A. Terwilliger, and B. C. Parker, "Surgical and medical applications of drones: A comprehensive review," *JSLS : Journal of the Society of Laparoendoscopic Surgeons*, vol. 22, no. 3, 2018.

[5] P. Doherty and P. Rudol, "A uav search and rescue scenario with human body detection and geolocalization," in *AI 2007: Advances in Artificial Intelligence*, M. A. Orgun and J. Thornton, Eds. Berlin, Heidelberg: Springer Berlin Heidelberg, 2007, pp. 1–13.

[6] J. Berni, P. Zarco-Tejada, L. Suárez, V. González-Dugo, and E. Fereres, "Remote sensing of vegetation from uav platforms using lightweight multispectral and thermal imaging sensors," *Int. Arch. Photogramm. Remote Sens. Spatial Inform. Sci*, vol. 38, no. 6, p. 6, 2009.

[7] Uber Elevate, "Fast-forwarding to a future of on-demand urban air transportation," 2016.

[8] B. Holmes, R. Parker, D. Stanley, P. McHugh, L. Garrow, P. Masson, and J. Olcott, "Nasa strategic framework for on-demand air mobility," *NASA Contractor Report NNL13AA08B, National Institute of Aerospace, Hampton, VA*, 2017.

[9] Y. Dobrev, M. Schuett, P. Hartmann, and D. Moormann, "Entwurf und validierung eines praezisionslandesystems fuer unbemannte tiltwing-fluggeraete," in *Deutscher Luft- und Raumfahrtkongress 2016, Institut fuer Flugsystemdynamik, RWTH Aachen University, Germany*, 2016.

[10] Novatel, in *NovAtel CORRECT - Optimize your positioning performance*, no. https://www.novatel.com/assets/Documents/Papers/NovAtelCORRECT-Brochure.pdf,lastaccessed: 07.02.20, December 2016.

[11] D. Peisen and B. Sawyer, "Heliport/vertiport mls precision approaches," in *SAIC Systems Control Technology Inc. and U.S. Department of Transportation, Federal Aviation Administration*, 1994.

[12] J. S. Wynn and T. W. McLain, "Visual servoing for multirotor precision landing in daylight and after-dark conditions," in *2019 International Conference on Unmanned Aircraft Systems (ICUAS)*, 2019, pp. 1242–1248.

[13] A. Marut, K. Wojtowicz, and K. Falkowski, "Aruco markers pose estimation in uav landing aid system," in *2019 IEEE 5th International Workshop on Metrology for AeroSpace (MetroAeroSpace)*, June 2019, pp. 261–266.

[14] Y. Jung, H. Bang, and D. Lee, "Robust marker tracking algorithm for precise uav vision-based autonomous landing," in *2015 15th International Conference on Control, Automation and Systems (ICCAS)*, Oct 2015, pp. 443–446.

[15] J. Wang and E. Olson, "AprilTag 2: Efficient and robust fiducial detection," in *Proceedings of the IEEE/RSJ International Conference on Intelligent Robots and Systems (IROS)*, October 2016.

[16] F. Romero-Ramirez, R. Muñoz-Salinas, and R. Medina-Carnicer, "Speeded up detection of squared fiducial markers," *Image and Vision Computing*, vol. 76, 2018.

[17] T. Krajník, M. Nitsche, J. Faigl, T. Duckett, M. Mejail, and L. Přeučil, "External localization system for mobile robotics," in *16th International Conference on Advanced Robotics (ICAR)*, Nov 2013.

[18] C. Toth, G. Jóźków, Z. Koppanyi, and D. Grejner-Brzezinska, "Positioning slow-moving platforms by uwb technology in gps-challenged areas," *Journal of Surveying Engineering*, vol. 143, 11 2017.

[19] K. Cisek, A. Zolich, K. Klausen, and T. A. Johansen, "Ultra-wide band real time location systems: Practical implementation and uav performance evaluation," in *2017 Workshop on Research, Education and Development of Unmanned Aerial Systems (RED-UAS)*, 2017, pp. 204–209.

[20] Y. Dobrev, Y. Dobrev, P. Gulden, M. Lipka, T. Pavlenko, D. Moormann, and M. Vossiek, "Radar-based high-accuracy 3d localization of uavs for landing in gnss-denied environments," in *2018 IEEE MTT-S International Conference on Microwaves for Intelligent Mobility (ICMIM)*, April 2018, pp. 1–4.

[21] P. Dabove, V. Di Pietra, M. Piras, A. A. Jabbar, and S. A. Kazim, "Indoor positioning using ultra-wide band (uwb) technologies: Positioning accuracies and sensors' performances," in *2018 IEEE/ION Position, Location and Navigation Symposium (PLANS)*, April 2018, pp. 175–184.

[22] C. Doer, R. Koenig, G. F. Trommer, and E. Stumpf, "Radar based autonomous precision takeoff and landing system for vtols in gnss denied environments," in *2020 International Conference on Unmanned Aircraft Systems (ICUAS)*, 2020.

[23] S. Khattak, C. Papachristos, and K. Alexis, "Marker based thermal-inertial localization for aerial robots in obscurant filled environments," in *Advances in Visual Computing*. Cham: Springer International Publishing, 2018, pp. 565–575.

[24] G. Bradski, "The OpenCV Library," *Dr. Dobb's Journal of Software Tools*, 2000.

[25] L. Meier, D. Honegger, and M. Pollefeys, "Px4: A node-based multithreaded open source robotics framework for deeply embedded platforms," in *2015 IEEE International Conference on Robotics and Automation (ICRA)*, 2015, pp. 6235–6240.

[26] R. S., *Computer vision: algorithms and applications*. Springer Science & Business Media, 2010.

[27] Stanford Artificial Intelligence Laboratory et al., "Robotic operating system." [Online]. Available: https://www.ros.org